ELSEVIER

Journal of Nuclear Materials 258–263 (1998) 1628–1633

journal of nuclear materials

Microstructural observation of helium implanted and creep ruptured Fe–25%Ni–15%Cr alloys containing various MC and MN formers

Norikazu Yamamoto *, Johsei Nagakawa, Yoshiharu Murase, Haruki Shiraishi

National Research Institute for Metals, 1-2-1, Sengen, Tsukuba, Ibaraki 305-0047, Japan

Abstract

Transmission electron microscopic observations have been carried out on Fe–25%Ni–15%Cr austenitic alloys with various MX (M = V, Ti, Nb, Zr; X = C, N) stabilizers after helium implantation and creep rupture at 923 K. It is shown that suppression of helium embrittlement can be achieved through a higher dispersion density of incoherent precipitates because of their high capability of bubble entrapment. A good agreement between the average distance of grain boundary bubbles exceeding the minimum critical size and the spacing of cavity traces on intergranularly fractured surfaces is obtained. This suggests that the enhancement of grain boundary decohesion by helium is a result of unstable growth of super-critical helium bubbles.

1. Introduction

It has been well recognized since the early proposition of Barnes [1] that helium can induce grain boundary embrittlement in neutron irradiated materials, and consequently deteriorate the mechanical properties at high temperatures. This degradation, the so-called helium embrittlement, is expected to arise more severely in future fusion devices in comparison with the other types of nuclear systems such as fast breeder and high temperature gas reactors, due to much larger amounts of helium generated in those devices. Accordingly, numerous efforts have been devoted to this phenomenon [2,3] in order to develop embrittlement-resistant candidates for first wall/blanket applications. From this standpoint, we have conducted mechanical testing on a variety of helium implanted materials, and recently demonstrated a link between the degree of helium embrittlement and precipitate microstructure through post helium implantation creep experiments on Fe–25%Ni–15%Cr austenitic alloys, that is, decreasing helium embrittlement with increasing the number density of precipitates in the matrix [4], as shown in Fig. 1.

The aim of the present work is to gain further information on helium embrittlement through detailed transmission electron microscope (TEM) observations and analysis on creep ruptured samples of austenitic alloys. More specifically, we would like to contribute to the development of high performance structural materials by clarifying the mechanism leading to embrittlement. For this purpose, special attention is focused on helium bubble microstructure, including bubble size distribution.

2. Experimental

The materials used are model Fe–25%Ni–15%Cr austenitic alloys modified only with MX (M = V, Ti, Nb, Zr; X = N, C) stabilizers, as shown in Table 1. Deliberate additions are shown by underlines in the table. Sample materials were given pre-implantation treatment, which was comprised of solution annealing, cold work and aging, for the purpose of controlling the microstructure. The first step of the treatment, solution annealing, brought about coarse $M_{23}C_6$ in Alloy 8203 and primary MX for the others resulting in a scattered dispersion at random orientations to the austenite matrix. In cases of the latter, this precipitation was followed by the formation of fine secondary MX particles, which

* Corresponding author. Tel.: +81 298 59 2844; fax: +81 298 59 2801; e-mail: yamamoto@nrim.go.jp.

0022-3115/98/$19.00
PII: S0022-3115(98)00226-8

Table 1
Chemical analysis of materials used (wt%)

Alloys	C	N	O	Ni	Cr	V	Ti	Nb	Zr	S	Fe
8201	0.064	0.001	0.007	24.98	14.82	–	0.24	–	–	0.003	Bal.
8202	0.072	0.001	0.010	24.70	14.49	–	–	–	0.41	0.002	Bal.
8203	0.109	0.001	0.006	24.52	15.02	0.47	–	–	–	0.002	Bal.
8204	0.010	0.058	0.010	24.52	15.06	0.40	–	–	–	0.003	Bal.
8206	0.076	0.001	0.007	24.58	14.82	–	0.19	0.10	–	0.003	Bal.
8207	0.114	0.001	0.007	24.54	15.05	0.47	0.09	–	–	0.005	Bal.

took place during aging at a higher number density with a simple cube-on-cube crystallographic habit to the matrix.

Helium was introduced into creep specimens, the gauge section of which was 10 mm long, 4 mm wide and 0.09 mm thick, at 923 K by α-particle irradiation at a cyclotron. To ensure homogeneous helium deposition all over the specimen depth, the energy of incident ions was adjusted by a rotating energy degrader consisting of nine wedge-shaped Al sheets. The accumulated helium concentration was about 50 appm. These specimens were, then, creep tested to failure also at 923 K with an applied stress of 120 MPa.

TEM samples were provided from a very near region of a ruptured portion. For the sake of statistical accuracy, all measurements of bubble size distributions were performed on more than three fields each from different grain locations. The sample thickness was determined by counting the number of equi-thickness fringes. The experimental details and creep test results were previously described in a companion paper [4].

3. Results and discussion

It is observed that for all alloys employed, helium implantation caused deterioration in terms of both creep rupture time and elongation, though the extent of the debasements differed from alloy to alloy, as illustrated in Fig. 1. In addition, a tendency toward intergranular fracture was widely promoted in every case. TEM examinations were made to clarify the causes of these helium effects.

3.1. Helium bubble distribution

Helium bubbles were found all over the specimen in nearly spherical or, less abundantly, polyhedral shapes for all materials. As formerly pointed out in Ti-modified austenitic steels [5–7], almost all of them were situated at extended lattice imperfections. Fig. 2 gives typical examples of such bubble-defect associations. Within grain interiors, bubbles were usually nucleated at interfaces of secondary phases which appeared before implantation.

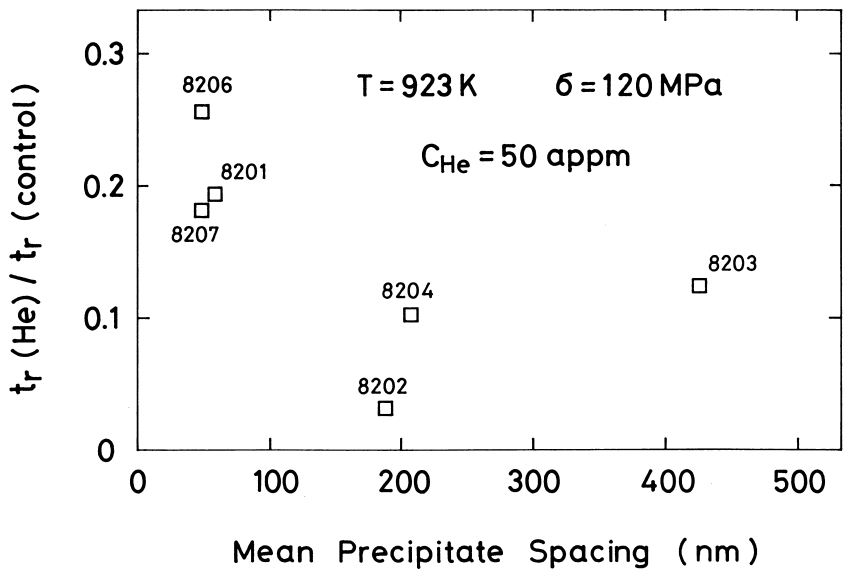

Fig. 1. Creep life ratio of helium implanted ($C_{He} = 50$ appm) specimens to unimplanted controls as a function of mean spacing of intragranular precipitates which were formed before implantation for 82 series alloys tested at 923 K, 120 MPa (Yamamoto et al. [4]).

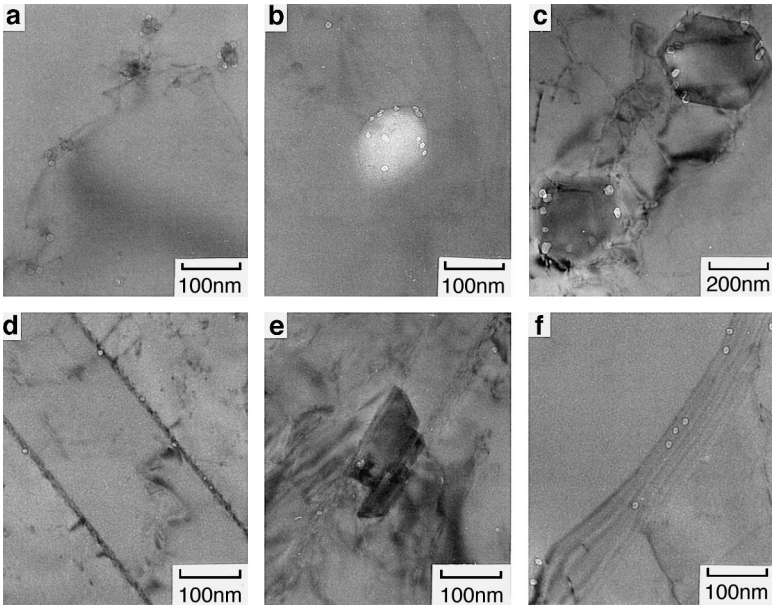

Fig. 2. TEM micrographs showing various helium bubble traps in 82 series alloys after post-implantation creep rupture ($T = 923$ K, $C_{He} = 50$ appm, $\sigma = 120$ MPa): (a) secondary MX and dislocation (Alloy 8202); (b) primary MX (Alloy 8204); (c) $M_{23}C_6$ (Alloy 8203); (d) twin boundary (Alloy 8206); (e) and (f) grain boundary (Alloys 8201 and 8204, respectively).

Incoherent precipitates, primary MX and $M_{23}C_6$, seem to have superior efficiency in trapping bubbles compared with semi-coherent ones (secondary MX), even though the majority of bubbles were attached at the latter due to their high density. This fact is in good agreement with earlier observations [7–10], showing higher bubble capture capabilities of less coherent phases.

Fig. 3 shows the difference in helium bubble segregation on precipitates formed at different time durations. As can be seen in the figure, the $M_{23}C_6$ which precipitated during implantation or creep, exhibited a lower capability of bubble trapping than that of secondary MX arising during the pre-implantation treatment. On the other hand, the former was less coherent than the latter. This rather unusual behavior of $M_{23}C_6$ can probably be attributed to termination of bubble nucleation at the early stages of hot implantation [11].

Results of statistical analyses on helium bubbles are summarized in Table 2. In all alloys, the mean size of intercrystalline bubbles was slightly larger than that of intragranular ones. The noticeably large size and low number density in Alloy 8203 most probably resulted from the absence of a high density dispersion of secondary MX in this alloy.

Therefore, it is concluded that the establishment of a high dispersion density with less coherent particles prior to helium introduction would effectively impede helium motion from grain interiors to grain boundaries through preferential bubble trapping and eventually reduce helium embrittlement.

3.2. Embrittlement mechanism

Fig. 4 exemplifies the typical failure morphology of grain boundary decohesion in helium implanted samples. As shown in the figure, faces of this fracture mode were often associated with small dimples, the spacings of which ranged from the order of hundreds of nm to several μm. This sponge-like structure, which is very common for helium embrittled materials, indicates that the fracture process is related to grain

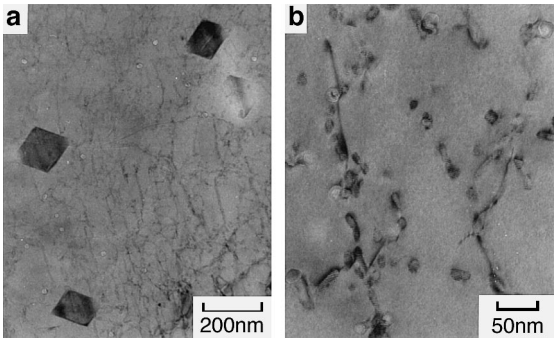

Fig. 3. TEM micrographs comparing helium bubble capture of different intragranular precipitates, which arose in different time periods, in Alloy 8207 after post-implantation creep rupture ($T = 923$ K, $C_{He} = 50$ appm, $\sigma = 120$ MPa, $t_r = 839$ ks): (a) $M_{23}C_6$ during or after implantation; (b) secondary MX (Moiré images) before implantation.

Table 2
Bubble microstructures in helium implanted and creep ruptured samples ($T = 923$ K, $C_{He} = 50$ appm)

Alloy	Creep data		Helium bubble			
	Applied stress (Mpa)	Rupture time (s)	Matrix		GB	
			Average radius (nm)	Number density (m^{-3})	Average radius (nm)	Number density (m^{-3})
8201	119	6.42×10^5	3.3	1.2×10^{20}	5.0	3.8×10^{13}
8202	119	7.99×10^4	4.9	3.0×10^{20}	6.6	3.4×10^{13}
8203	119	9.61×10^4	17.1	1.7×10^{19}	20.4	2.7×10^{13}
8204	119	1.71×10^5	3.9	4.7×10^{19}	5.6	5.6×10^{13}
8206	118	1.07×10^6	3.6	2.7×10^{20}	5.3	5.8×10^{13}
8207	120	8.39×10^5	5.9	1.6×10^{20}	7.7	4.6×10^{13}

boundary helium bubbles. In order to determine the validity of this postulate, we estimated the minimum critical radius, in a method described below, and compared it with observed bubble size distributions at grain boundaries.

The concept of the minimum critical radius, which was first introduced by Hyam and Sumner [12], means the limit beyond which bubbles become energetically unstable and continue to grow up to fracture. We have evaluated it through direct computation of the bubble growth rate by using the following expression [13]:

$$\frac{\partial r}{\partial t} \propto C_{vB}^{e} \exp\left(\frac{\Omega\sigma_N}{kT}\right) \times \left[1 - \exp\left\{\frac{\Omega}{kT}\left(\frac{2\gamma}{r} - P_g - \sigma_N\right)\right\}\right]. \quad (1)$$

Here, r is the bubble radius, C_{vB}^{e} the equilibrium vacancy concentration in the grain boundary, Ω the atomic volume, σ_N is the stress normal to the boundary, γ the surface energy, P_g the gas pressure within the bubble and kT has its usual meaning. In the calculation of P_g, a hard sphere equation of state with Lenard–Jones potential [14] was adopted, instead of the usual ideal gas law, because bubble pressures handled here are ordinarily very high, reaching to several GPa.

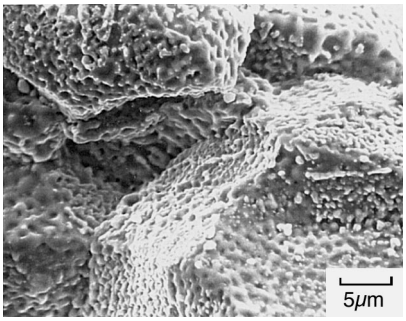

Fig. 4. SEM fractograph showing typical "sponge" structure on intergranularly fractured facets after post-implantation creep rupture; photo was taken on Alloy 8207 ($T = 923$ K, $C_{He} = 50$ appm, $\sigma = 120$ MPa, $t_r = 839$ ks).

Fig. 5 illustrates the result of calculations with the assumption that $\gamma = 1.5$ J/m^2, as an example. In stressed conditions (during creep), $r_c^* = 17.2$ nm is obtained for the minimum critical radius along with the broken line in the figure. However, the growth rate–radius relationship is converted to the solid line following a bold arrow in Fig. 5 after stress relief (creep rupture). The bubble shrinks toward a newly introduced stable (and equilibrium) state of $r_c^0 = 10.8$ nm by emitting vacancies. We utilized this "relaxed" critical radius [15] for analyses described below, since TEM observations were made on stress-free samples.

Fig. 6 shows examples of intercrystalline bubble size distributions with r_c^0 at $\gamma = 1.5$ J/m^2. Bubbles larger than r_c^0 should grow indefinitely in an unstable manner by the mechanisms, such as vacancy condensation and creep-constrained growth. Table 3 gives the average distances of grain boundary bubbles with super-critical radii in cases of $\gamma = 2.0$, 1.5 and 1.0 J/m^2. These values usually stay within the order of hundreds of nm, and coincide with the spacings of cavity traces on the surfaces of intergranular fracture mentioned above. This correspondence possibly mirrors grain boundary separation led by the instability of helium bubbles.

4. Conclusions

Detailed TEM examination on helium implanted ($T = 923$ K, $C_{He} = 50$ appm) and creep ruptured ($T = 923$ K, $\sigma = 120$ MPa) Fe–25%Ni–15%Cr alloys merely modified with MX (M = V, Ti, Nb, Zr; X = N, C) formers led to the following conclusions:

(1) Less coherent precipitates introduced before helium implantation efficiently functioned as bubble nucleation sites. It is therefore expected that mechanical

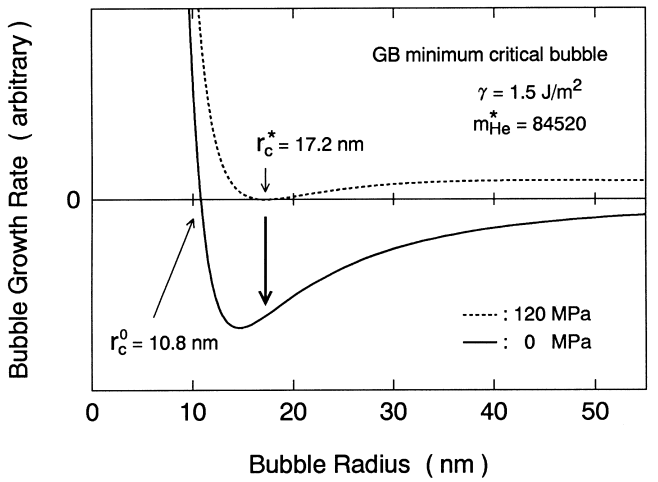

Fig. 5. Computed growth rate of an intergranular helium bubble with the minimum critical radius as a function of bubble radius using a hard sphere equation of state with Lenard-Jones potential.

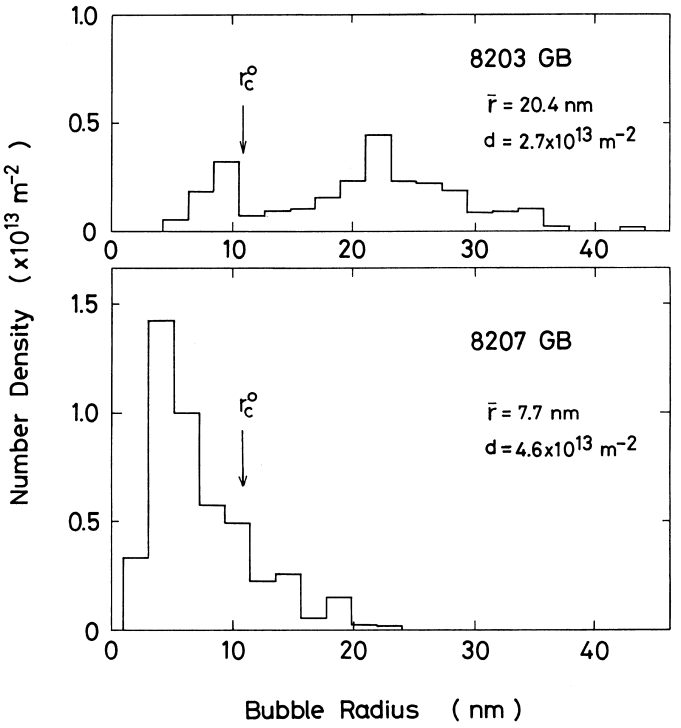

Fig. 6. Representative helium bubble size distributions at grain boundaries in 82 series alloys after post-implantation creep rupture ($T = 923$ K, $C_{He} = 50$ appm, $\sigma = 120$ MPa).

deterioration induced by helium would be suppressed by the presence of finely dispersed incoherent particles preceding helium introduction.

(2) From measurements on the size distribution of grain boundary helium bubbles and fractographical examinations on ruptured surfaces, good correspondence between the spacing of bubbles beyond the minimum critical size and that of dimples on intergranularly fractured regions is obtained. This fact probably reflects a fracture process governed by unstable growth of bubbles with super-critical sizes at grain boundaries.

Table 3
Mean spacing of grain boundary bubbles with over critical sizes in helium implanted and creep ruptured samples ($T = 923$ K, $C_{He} = 50$ appm, $\sigma = 120$ MPa)

Alloy	Mean spacing of over critical bubbles at GBs (nm)		
	$\gamma = 2.0$ J/m^2	$\gamma = 1.5$ J/m^2	$\gamma = 1.0$ J/m^2
8201	9.9×10^2	7.2×10^2	4.3×10^2
8202	4.8×10^2	4.7×10^2	4.2×10^2
8203	2.3×10^2	2.2×10^2	2.0×10^2
8204	–	–	3.6×10^2
8206	7.5×10^2	6.3×10^2	3.1×10^2
8207	4.7×10^2	3.3×10^2	2.3×10^2

References

[1] R.S. Barnes, Nature 206 (1965) 1307.
[2] H. Ullmaier, Nucl. Fusion 24 (1984) 1039.
[3] L.K. Mansur, M.L. Grossbeck, J. Nucl. Mater. 155–157 (1988) 130.
[4] N. Yamamoto, J. Nagakawa, H. Shiraishi, J. Nucl. Mater. 226 (1995) 185.
[5] P.J. Maziasz, Scripta Metall. 14 (1980) 1251.
[6] W. Kesternich, Radiat. Eff. 78 (1983) 261.
[7] N. Yamamoto, H. Shiraishi, H. Kamitsubo, I. Kohno, T. Shikata, A. Hishinuma, J. Nucl. Mater. 141–143 (1986) 486.
[8] A. Czyrska-Filemonowicz, W. Kesternich, J. Nucl. Mater. 137 (1985) 33.
[9] N. Yamamoto, J. Nagakawa, H. Shiraishi, H. Kamitsubo, I. Kohno, T. Shikata, J. Nucl. Sci. Technol. 28 (1991) 1001.
[10] H. Schroeder, Y. Dai, J. Nucl. Mater. 191–194 (1992) 781.
[11] H. Ullmaier, Radiat. Eff. 101 (1986) 147.
[12] E.D. Hyam, G. Sumner, in: Proceedings of the International Symposium on Radiation Damage in Solids, vol.1, IAEA, Vienna, 1962, p. 323.
[13] R. Bullough, S.M. Murphy, J. Nucl. Mater. 133/134 (1985) 92.
[14] I.R. Brearley, D.A. MacInnes, J. Nucl. Mater. 95 (1980) 239.
[15] H. Trinkaus, H. Ullmaier, J. Nucl. Mater. 155–157 (1988) 148.